ANALYSIS OF BENDING IN PARTIALLY-BONDED STRUCTURES OF ELECTROADHESIVE POLYMERS

by

Carlos Arguero

B.S. in Mechanical Engineering, University of Pittsburgh, 2014

Submitted to the Graduate Faculty of

Swanson School of Engineering in partial fulfillment

of the requirements for the degree of

Master of Science in Mechanical Engineering

University of Pittsburgh

2017

UNIVERSITY OF PITTSBURGH

SWANSON SCHOOL OF ENGINEERING

This thesis was presented

by

Carlos Arguero

It was defended on

August 24, 2017

and approved by

William W. Clark, Ph.D., Professor, Department of Mechanical Engineering and Materials Science

Jeffrey Vipperman, Ph.D., Professor, Department of Mechanical Engineering and Materials Science

Tara Meyer, Ph.D., Professor, Chemistry Department

Thesis Advisor: William W. Clark, Ph.D., Professor,

Department of Mechanical Engineering and Materials Science

ANALYSIS OF BENDING IN PARTIALLY-BONDED STRUCTURES OF ELECTROADHESIVE POLYMERS

Carlos Arguero, M.S.

University of Pittsburgh, 2017

Electroadhesive polymers are a variety of polymers that experience attractive forces under applied voltages and currents. By arranging these polymers in a layered beam-type structure, these attractive forces can be exploited to create an increase in effective bending stiffness. In such a structure, the effective stiffness depends on the electrical signal being applied; when no voltage is present, for example, the structure behaves simply as a stack of inert polymers, analogous to multiple unbonded beams. However, as the applied voltage increases, the effective stiffness increases measurably. In theory, the stiffness would continue to increase with respect to voltage until the structure performed as if it were a single beam of uniform composition. While this increase in performance would suggest many useful applications of such materials, the precise nature of this behavior is unknown. Of particular interest is how the stiffness increases during the 'intermediate' composite-beam stage, i.e. before the uniform-beam performance threshold is reached. Characterization of this intermediate voltage-stiffness relationship forms the basis of this thesis. The first analysis is an extension of 'first principles,' and is based wholly on applying simple mechanics of beams to empirical results. Following this initial analysis, a more detailed exploration of available literature attempts to survey available theories and methods for measuring stiffness in partially-bonded beam structures. Finally, the most promising of the available methods is/are selected for further experimental analysis, and suggestions are put forward as a basis for future work.

TABLE OF CONTENTS

LIST OF TABLES

LIST OF FIGURES

PREFACE

I would like to acknowledge the invaluable contributions of the many individuals who helped me along the path to completing my thesis. First and foremost, I would like to thank my advisor, Dr. William Clark, both for initially brining me into the project, and for providing guidance and expertise to help me see it through. Acknowledgements are also due to Dr. Tara Meyer of the Chemistry department for her role in the overall research initiative. I would also like to thank Dr. Jeffrey Auletta of the Chemistry Department for his essential contributions to the experimental design and data collection, as well as his knowledge of the materials being examined. Further thanks are extended to Colin Ladd, whose work provided a basis for my analysis, and to Ehsan Qaium, who assisted in the creation of our sample polymers. Thanks are also owed to Dr. Tevis Jacobs and Luke Thimons for their insight into the workings of adhesion, especially on the microscale. Finally, I would like to thank my parents for their support, both financial and moral.

1.0 INTRODUCTION

A dark figure crouches on a moonlit rooftop, searching the streets below. Spotting his target, he unfurls a pair of light, flexible wings from a specially-made suit and jumps; the wings stiffen, providing the lift to allow him to glide gracefully and silently to the ground behind his quarry. Suddenly, floodlights blink on, and shots ring out from a dozen directions. Crouching down, our hero wraps his wings around himself, the bullets deflecting harmlessly off the now-rigid shell that mere moments before had borne him aloft. The barrage over, he stands, his cape returning to its flowing, fabric-like state; a few minor burns the only sign of damage.

Popular culture and science alike have long sought after ‘magic’ materials like our hero’s cape; materials that can change their properties on the fly, altering their color, shape, stiffness, and more. Only in the last few decades has the ‘polymer revolution’ of modern materials science finally allowed these dreams to approach reality; many novel applications have been enabled by a constantly growing catalog of polymers. Among these materials are electroadhesive polymers, which demonstrate variable levels of adhesion when exposed to electric currents. By stacking together layers of these polymers, the stiffness of the overall structure can be increased or decreased by applying a particular electric signal; in this paper, we explore how to properly analyze and model the performance of such structures.

2.0 BACKGROUND AND LITERATURE REVIEW

This work was performed in collaboration with the Meyer Group (in particular with Dr. Jeffrey Auletta and Colin Ladd) of the University of Pittsburgh's Chemistry Department. Ladd's work focused on the empirical characterization of the behavior of electroadhesive polymers under applied voltages, including performing three point bending tests of polymer beams to determine flexural stiffness. However, his experiment was limited to beams consisting of two polymer layers exposed to a limited range of voltages. To improve our understanding of the mechanics at play and to guide future polymer structure designs, we wish to develop a generalized theoretical model for modulus at any voltage, for any beam-like polymer structure.

2.1 LITERATURE REVIEW

2.1.1 The Coulomb Force

Any discussion of electroadhesion must begin with a discussion of the Coulomb force (sometimes also referred to as the Coulomb effect). The Coulomb force is the outcome of Coulomb's Law; originally published in the late 18^{th} century and reprinted many times since, the law states that the force between two charged particles is proportionate to the product of the magnitudes of the charges, and inversely proportionate to the square of the distance between the

charges [e.g. Halliday *et al.* 2007]. Whether the force is attractive or repulsive depends on the sign of the charges; opposite charges attract, similar charges repulse. While the traditional formulation of Coulomb's Law is for point particles, it can be extended to any geometry of charges. In the case of parallel charged sheets or plates with an intervening dielectric layer, such as our layered structure, we must make some alterations to account for material properties of the layers, as well as accounting for the planar distribution of charge. Thus, in our case the Coulomb force can be expressed as:

$$\boldsymbol{F_C = \frac{A}{2}\varepsilon_0\left(\frac{k_r V}{d}\right)^2} \quad (1)$$

where A is the area of the electrodes, ε_0 is the free-space permittivity, k_r is the dielectric constant of the dielectric layer, V is the applied voltage, and d is the thickness of the dielectric layer (the distance between the electrodes) [Halliday *et al.*, 2007]. Under an applied voltage, dipoles within the dielectric layer align; for the Coulomb effect to strongly manifest the resistance within the dielectric must be large compared to the resistance at the contact between layers. This causes the voltage drop to occur over the entire dielectric thickness *d.*

2.1.2 The Johnsen-Rahbek Effect

Though it is the most fundamental of electroadhesive effects, the Coulomb force is not the only force at play. Essential to the effectiveness of the layered polymer structure is the Johnsen-Rahbek (J-R) Effect, an electroadhesive force resulting from imperfections in real systems that was first demonstrated empirically by the eponymous Johnsen and Rahbek in 1923. A refined theoretical model and extension of the initial principles was published in 1969 by Atkinson [R. Atkinson, 1969]. In a material exhibiting the J-R effect, an applied voltage causes mobile

charges to migrate to the surface of the dielectric layer. As a result of surface roughness, contact on the surface of the dielectric is not complete; the irregularity of the layer's surface creates gaps between areas of contact. The effective area of contact depends on the proportion of total area occupied by gaps. When the contact resistance at these points is much greater than the resistance of the dielectric layer, then the mobile charges accumulate at the gaps; as more charge moves to the layer's surface, these gaps become areas of strong electrical attraction, thus creating the J-R effect. The accumulation of these mobile charge carriers is a key difference from the Coulomb effect, and their presence is governed by the comparative resistances of the contact points and the dielectric layer.

We can express the strength of the J-R effect using a similar form to the Coulomb force:

$$F_{JR} = \frac{A_{eff}}{2} \varepsilon_0 \left(\frac{k_g V_{eff}}{g}\right)^2 \quad (2)$$

Here, A_{eff} is the effective contact area between the dielectric layers, accounting only for those areas of direct surface-to-surface contact resulting from surface roughness. Similarly, k_g is the dielectric constant of the gaps between layers (usually represented as air or vacuum with a value equal to one), g is the gap distance, and V_{eff} is the effective applied voltage. This effective voltage varies with respect to the contact resistance of the effective contact area, which can increase or decrease as more of the surface of the dielectric layers comes into contact.

All real systems experience both Coulomb and J-R effects to a certain degree, with the dominant effect largely depending on the resistances of the contact areas and dielectric layers, as discussed above. In a Coulomb-dominant material, high dielectric resistance produces a voltage drop over the entire dielectric thickness *d*; in a J-R-dominant material, high contact resistance causes the voltage drop to be concentrated over gaps with size g. Qin and McTeer provide a useful comparison of the Coulomb and J-R effects, using examples from their work with

electrostatic chucks [Qin & McTeer, 2007]. They observe that, all other conditions being equal, the dielectric resistivity governs which force is dominant, and that the dominance crossover occurs at a given resistivity value (dependent upon other factors). However, they note that in many applications, the J-R effect can strongly manifest due to the difference between the size of the gap between the dielectric layers g and the distance between electrodes d; when $g<<d$ the J-R force is particularly dominant.

Consider the situation shown in Figure 1, representing the gaps that can occur between dielectic layers which are in contact. Two parallel electrodes (hatched areas) are separated by one or more dielectric layers (dotted areas). The surface roughness of the dielectrics creates areas of direct contact surrounded by gaps. In the left Coulomb-dominant scenario, the majority of the distance d between the electrodes is occupied by the relative thickness of the dielectric layer, leaving only small gaps between the upper electrode and the dielectric layer. Dipoles within the dielectric later align to the applied voltage, and the high resistivity of the dielectric causes voltage to drop over the entire distance d. In the right scenario, high contact resistance and low dielectric resistance causes charge to accumulate at the gaps (size g) between dielectric surfaces. This causes the J-R effect to manifest more strongly; the smaller the gap, the stronger the force.

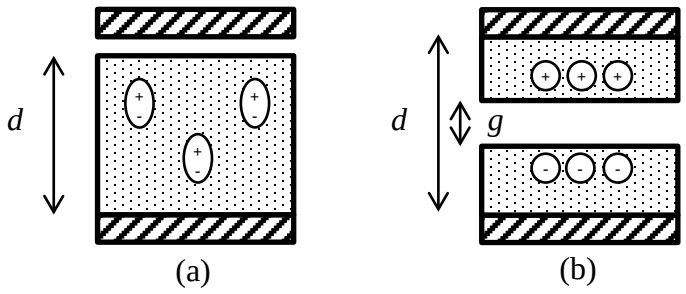

Figure 1. In (a), a dielectric layer with high resistivity causes Coulomb effects to manifest. Dipoles align with applied voltage. In (b), high contact resistivity causes charge accumulation at the gap. This creates J-R effects.

Qin and McTeer note that the relationship between gap size and manifested force can be quite powerful; in particular, they conclude that the extreme sensitivity of J-R effects to gap size and

material and environmental conditions verges on the problematic for their application, electrostatic chucks. Nevertheless, they claim that exploiting J-R effects offers higher performance than Coulomb effects; much higher attractive forces can be achieved at substantially lower voltages.

While a popular subject of investigation, the discussion of applications for J-R effects in literature is largely dominated by the electrostatic chuck perspective covered by Qin and McTeer. In the context of binding material layers, especially polymers, a class of materials known as Electro-Bonded Laminates has been explored in literature; while much of the groundwork is similar to the voltage dependent J-R interaction examined by Ladd, the discussion never explicitly links to the J-R effect [L. Di Lillo *et al*., 2011]. However, despite the relative novelty of the analysis, given the combination of electrical properties and the surface roughness of the polymers investigated by Ladd, the J-R effect appears to be the dominant electroadhesive effect.

2.2 PREVIOUS RESEARCH

The initial dataset used in modeling phenomena was taken with permission from the three-point bending experiments performed by Ladd [Ladd, 2015]. Ladd's work studied four polymers; they are discussed in detail below.

2.2.1 Poly(ethylene-*co*-acrylic) Acid

Solutions derived from Poly(ethylene-*co*-acrylic) acid (PEAA) were highlighted as potential electroadhesive polymers in a patent filed by Cipriano and Longoria [Cipriano & Longoria, 1996]. Ladd and associates adopted one such solution, and developed two additional solutions from PEAA. As it is the foundation upon which the other experimental polymers were based, unaltered PEAA was introduced as a control polymer; by itself it is not electroadhesive and should experience no change in stiffness as voltage is changed.

2.2.2 Tetramethylammonium Hydroxide

A solution of PEAA with Tetramethylammonium hydroxide (TMAH) was the polymer design adopted by Ladd and associates from Cipriano and Longoria. The PEAA-TMAH solution was created by dissolving beads of PEAA in an aqueous solution of TMAH, allowing the neutralization of the acrylic acid in the PEAA.

2.2.3 Tetraethylammonium Hydroxide

The first novel PEAA-base polymer solution examined by Ladd was a solution with Tetraethylammonium hydroxide (TEAH). The same fabrication procedure was employed as the PEAA-TMAH solution.

2.2.4 Tetrapropylammonium Hydroxide

A solution of Tetrapropylammonium hydroxide (TPAH) with PEAA was the second novel polymer solution analyzed by Ladd. As before, the same fabrication procedure was employed as with the PEAA-TMAH solution.

2.2.5 Experimental Methods

Samples of the above polymers were attached to rectangular aluminum electrodes (thickness 0.127mm), with typical final dimensions of 80 x 19 mm. To affix a sample of each polymer solution to the aluminum electrodes, a bead of solution was applied to an electrode and then smoothed with a pulldown bar. After smoothing, the polymer was baked in a 60º C oven until the consistency slightly firmed; this process of application, smoothing, and baking was repeated until the thickness of the polymer on the electrode was approximately 0.60 mm. A final baking process then dried the sample to the touch, and razor blade was used to trim any polymer spillage. One such polymer-electrode pair constitutes a single layer. Two layers were then stacked together with the polymer sides in contact to form the complete layered beam structure used in the three point bend test. A diagram of such a sample is shown in Figure 2.

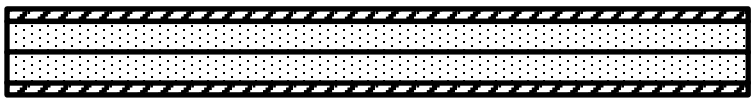

Figure 2. Layered structure of polymer samples (dotted areas) and electrodes (striped areas) (not to scale).

Samples of each variety of polymer were prepared for testing by conditioning at 11% relative humidity for 72 hours prior to data collection; enough samples were prepared such that measurements could be taken in triplicate to ensure repeatability. Each sample was affixed to a custom-built three-point-bending device, maintained by the author of this paper. The device utilized a two-axis platen controlled by stepper motors for positioning of samples under the test head. The test head incorporated a cylindrical contact zone positioned via stepper motor to provide a constant rate of deformation to the sample, and a 10-lb load cell to measure the bending force required. The sample was also connected to a high voltage supply, which was used to increase the voltage in the sample in 50 volt increments from zero to 450 volts. At each voltage, load and deflection in the sample were measured; this data was used to calculate the bending stiffness (equivalent to the ratio of force applied to maximum deflection) for each sample. From the measured stiffness, the effective rigidity (EI, where E is the elastic modulus of the beam and I is the area moment of inertia) of the beam was then calculated.

2.3 PREVIOUS RESULTS

A summary of the rigidity results are shown in Table 1, while Figure 3 shows the evolution of the rigidity with respect to voltage.

Table 1. Effective rigidity results from Ladd with standard deviations.

	Effective rigidity ± Standard Deviation (Nm^2)			
Applied Potential (V)	**PEAA**	**PEAA-TMAH**	**PEAA-TEAH**	**PEAA-TPAH**
0	1169.0 ± 51.7	529.8 ± 7.6	339.3 ± 7.4	266.6 ± 8.2
50	1130.0 ± 34.4	549.1 ± 13.6	370.4 ± 20.4	316.1 ± 22.7
100	1117.2 ± 44.4	568.7 ± 6.8	375.8 ± 5.5	328.4 ± 6.1
150	1085.8 ± 19.1	548.3 ± 18.4	367.1 ± 10.8	337.1 ± 12.0
200	1090.2 ± 47.6	552.2 ± 8.7	411.0 ± 29.1	365.3 ± 32.4
250	1111.0 ± 39.2	557.3 ± 6.1	391.2 ± 45.7	366.3 ± 50.9
300	1112.0 ± 46.5	516.5 ± 8.6	456.1 ± 15.6	361.1 ± 17.4
350	1045.4 ± 15.8	561.0 ± 36.5	514.4 ± 43.9	432.7 ± 48.9
400	1069.8 ± 57.6	627.2 ± 62.5	576.2 ± 24.3	464.6 ± 27.1
450	1039.0 ± 23.2	795.4 ± 77.6	677.8 ± 55.6	650.3 ± 61.9

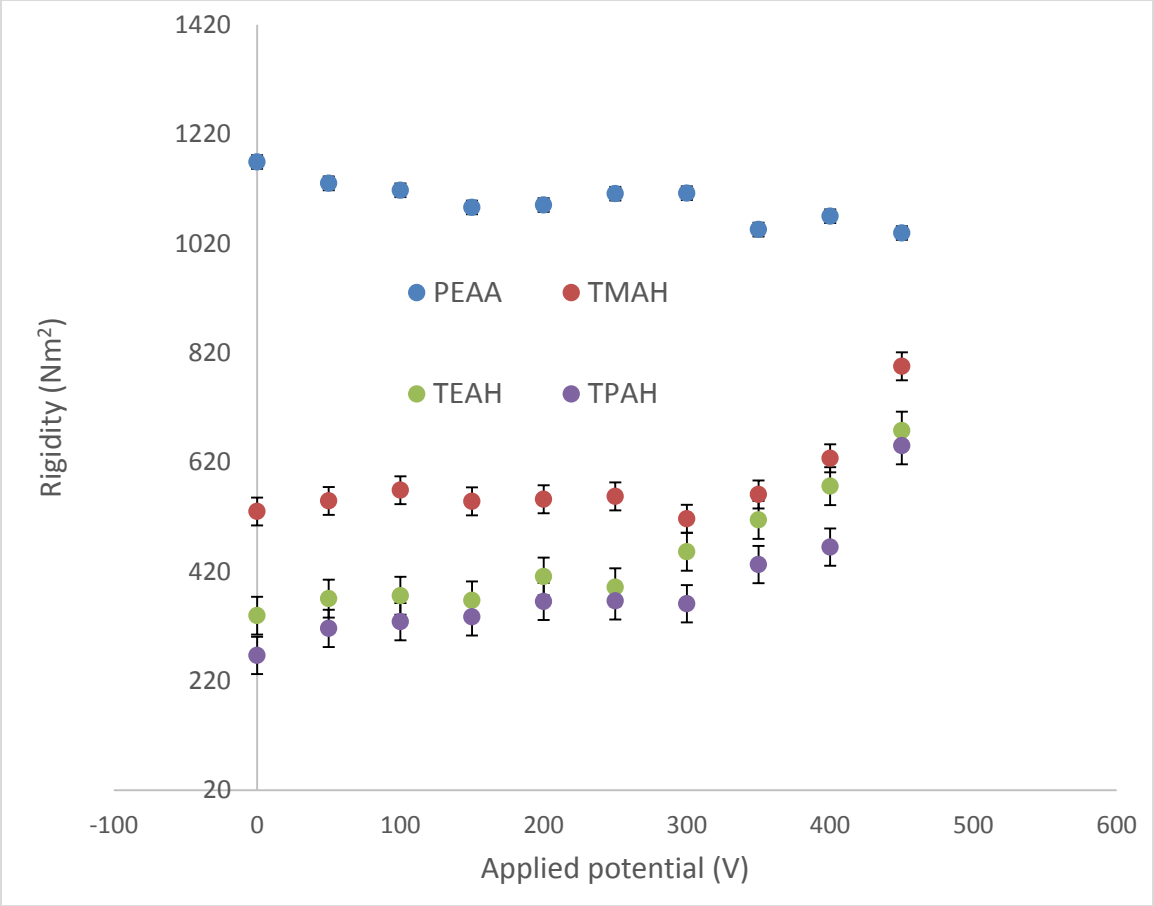

Figure 3. Rigidity plotted against applied voltage.

2.4 CHARACTERIZATION OF PREVIOUS RESULTS

Below we consider the performance of each polymer, as well as a general summary of the behavior of the polymer.

2.4.1 Poly(ethylene-*co*-acrylic) Acid

The data collected from PEAA samples by Ladd shows a modest (approximately 10%) decay in rigidity as voltage increases; this decrease is attributed to the polymer samples physically decaying over the course of the experimental procedure and is not indicative of a stiffness increase or decrease at higher voltages.

2.4.2 Tetramethylammonium Hydroxide

PEAA-TMAH shows the greatest initial rigidity, but it also increases in rigidity the slowest with respect to voltage increases; it does not experience a significant rigidity increase until approximately 350V. The final measured rigidity for PEAA-TMAH shows a 150% increase over the zero-volt rigidity. If we assume that, like the PEAA, there is an approximately 10% drop in stiffness due to sample deterioration over the course of data collection, then the actual stiffness increase may be more substantial than indicated.

2.4.3 Tetraethylammonium Hydroxide

Samples of PEAA-TEAH demonstrated zero-voltage flexural moduli that fell in between the other test polymers, and a rigidity increase of 200% at maximum voltage. However, PEAA-TEAH also showed the earliest increase in rigidity with respect to voltage; increased rigidity occurred at a voltage approximately 50-75V lower than the other polymers.

2.4.4 Tetrapropylammonium Hydroxide

The zero-voltage moduli exhibited by samples of PEAA-TPAH were the lowest among all the test polymers, but showed the most rapid rise after beginning to increase at around 300V. At full voltage, PEAA-TPAH samples demonstrated a 250% rigidity increase.

2.4.5 Summary of Previous Findings

In Ladd and associates' comparison of PEAA and three derivative electroadhesive polymers, all non-control solutions demonstrated increased stiffness with voltage. PEAA-TMAH demonstrated the greatest initial effective rigidity, but also the latest inflection point and smallest relative increase in effective rigidity at maximum voltage. Samples of PEAA-TEAH showed intermediate initial moduli and an average relative increase with the earliest inflection point. Finally, PEAA-TPAH samples showed the smallest initial moduli, but experienced the greatest proportional increase after an intermediate inflection point.

2.5 SUMMARY

The work performed by Ladd and associates focused on the creation of polymers demonstrating the effects discussed in section 2.1. In this they succeeded; leveraging the Coulomb and J-R effects produced rigidity increases of varying degrees in layered beam structures constructed of polymer samples. Due to the configuration of the samples (namely, the electrical properties of the polymer samples, and their surface roughness), the J-R effect provides the majority of the

binding force between layers. However, while Ladd's work shows the existence of electroadhesive effects, it does not quantify them in such a way as to allow for calculation of expected flexural rigidity prior to experimental testing. To that end, in this thesis we combine empirical analysis of Ladd's data with application of engineering principles to develop empirical and theoretical models for the same type of layered polymer structures; we also attempt to extend this model to any generalized layered polymer beam.

3.0 ANALYTICAL DEVELOPMENT OF A MODEL

Because of electroadhesive effects, the flexural rigidity of our layered polymer structure varies with voltage. We anticipate three distinct modes of behavior corresponding to different voltage ranges. When no voltage is present, there are no electroadhesive effects, and we expect the structure to behave as a set of unbonded beams. After some threshold voltage, we expect the structure to behave as a single composite beam. These cases are easily solvable from elementary beam theory, a well-known solution for the characterization of beams undergoing three-point bending; it forms the basis of our initial exploration, as shown in the following sections. The third and final behavior mode corresponds to the performance of the structure at intermediate voltages; this remains unknown and forms the motivation for the empirical model and the key focus of this thesis.

3.1 ELEMENTARY BEAM BENDING

We first turn our attention to a discussion of Elementary (a.k.a. Euler-Bernoulli or Engineering) Beam Theory; specifically a derivation of beam deflection in terms of forces and beam dimensions. We work the problem in two parts – a derivation of the necessary beam conditions for elementary theory to apply, and a solution of the bending equation for midpoint deflection. While elementary bending theory is discussed in numerous texts, we choose to base our solution

on the methods presented in Ugural and Fenster's *Advanced Strength and Applied Elasticity* [Ugural & Fenster, 2003].

Suppose we have a long, narrow beam with vertical symmetry (that is, symmetrical across the xy-plane, see Figure 4). The beam experiences a point load *P* at its midpoint.

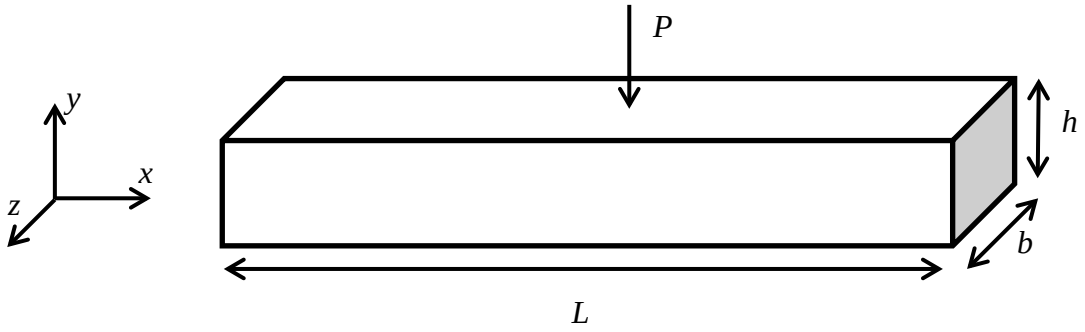

Figure 4. Diagram of a long, narrow beam with a rectangular cross section.

The beam is simply supported at its endpoints. We use conventional axial definitions, with *x* indicating position on the x-axis and *y* indicating y-position. Additionally, *u* represents x-axis deformation, while *v* represents y-axis deformation. Elementary theory makes the following assertions as to the normal (ε) and shear (γ) strain conditions in the beam:

$$\varepsilon_x = \frac{\sigma_x}{E} \qquad (3.1) \qquad \gamma_{xy} = \frac{du}{dy} + \frac{dv}{dx} = 0 \qquad (3.2)$$

$$\varepsilon_y = \frac{dv}{dy} = 0 \qquad (3.3) \qquad \gamma_{yz} = 0 \qquad (3.4)$$

$$\varepsilon_z = 0 \qquad (3.5) \qquad \gamma_{zx} = 0 \qquad (3.6)$$

The x-axis normal strain equation (Equation 3.1) reflects the stress-strain relationship for narrow beams. The y-axis normal strain equation ensures that all points at a particular x-axis position undergo the same deformation; that is, any cross-section deforms uniformly, without separation. When taken together with the xy-plane shear strain equation, this guarantees that vertical planar sections (cross-sections of the beam along the x-axis) remain planar during

bending. This is central to the construction of elementary bending theory. The three remaining zero-strain conditions indicate that the beam is subjected to plane stress.

Having established the basic prerequisite conditions of elementary theory, we now turn our attention to the principle governing equation for beam behavior. The bending of a beam in the y-direction along its x-axis is expressed as:

$$\frac{d^2v}{dx^2} = \frac{M_z}{EI_z} \tag{4}$$

In this equation, M_z represents the moment about the z-axis, and I_z represents the second moment of inertia about the z-axis. For a simply-supported beam with a point load P at its center, we can substitute the expression for the moment in the beam from $x = 0$ to $\frac{L}{2}$ as:

$$\frac{d^2v}{dx^2} = \frac{M_z}{EI_z} = \frac{Px}{2EI_z} \tag{5}$$

Integrating, we find the slope in the beam at location x:

$$EI_z\frac{dv}{dx} = \int_0^x M_z dx + C_1 = \frac{Px^2}{4} + C_1 \tag{6}$$

Ignoring the generated constant term for now and integrating again, we find the deflection:

$$EI_z v = \int_0^x dx \int_0^x M_z\, dx + C_1 x + C_2 = \frac{Px^3}{12} + C_1 x + C_2 \tag{7}$$

We are now in a position to solve for constants C_1 and C_2 using the boundary conditions of the beam. We have two conditions and two unknowns, so a unique solution exists. Our first condition is at the end of the beam corresponding to $x = 0$. We know that due to the simple support, the deflection v must also be zero. Substituting these values, we see that C_2 must be zero. Our second boundary condition comes from our knowledge that the peak deflection occurs at the midpoint of the beam, directly under the load. We know then that the slope of the beam (the derivative of deflection) must be zero at $x = \frac{L}{2}$. Substituting, we find that C_1 must satisfy:

$$-\frac{PL^2}{16} = C_1 \tag{8}$$

Now, we assemble the entire equation and solve for the deflection at the midpoint:

$$EI_z v = \frac{Px^3}{12} - \frac{PL^2}{16}x \tag{9}$$

$$EI_z v = \frac{P}{12}\left(\frac{L^3}{8}\right) - \frac{PL^2}{16}\left(\frac{L}{2}\right) \tag{10}$$

$$EI_z v = \frac{PL^3}{96} - \frac{PL^3}{32} \tag{11}$$

$$EI_z v = -\frac{2PL^3}{96} \tag{12}$$

Rearranging so that the deflection *v* is alone on the left hand side, we arrive at our solution:

$$v = -\frac{PL^3}{48EI_z} \tag{13}$$

Before further developing this expression, we make a few symbolic changes. For simplicity, we choose to change our sign convention; deflection downwards now carries a positive sign. We also change some of our variables; we use δ for the maximum deflection instead of *v*, and drop the subscript from the second moment of inertia *I*. Our relabeled solution takes the following form.

$$\delta = \frac{PL^3}{48EI} \tag{14}$$

For a sample of known geometry, finding the modulus is a trivial reorganization of the above.

$$E = \frac{PL^3}{48\delta I} \tag{15}$$

The second moment of inertia of a rectangular cross section is shown below. ,

$$I = \frac{bh^3}{12} \tag{16}$$

Were we solving for modulus, we could substitute for physical quantities as follows:

$$E = \frac{12PL^3}{48\delta bh^3} = \frac{PL^3}{4\delta bh^3} \tag{17}$$

However, in this case we can adopt a simplified expression for rigidity:

$$EI = \frac{PL^3}{48\delta} \tag{18}$$

For an ordinary beam, the rigidity can now be solved for directly. However, due to our expected three performance regimes (unbonded, partially bonded, and fully bonded), further analysis is required. In the sections below, we examine the two cases with which elementary bending theory applies directly; however, the behavior of the structure at intermediate voltages remains unknown.

In order to perform the following analysis, we make several requisite assumptions; each polymer sample is treated as a simple beam undergoing pure bending, and we assume there are no mechanical linkages between polymer samples. Furthermore, we assume an ideal test setup; the polymer samples are perfectly aligned, the beam is loaded at its precise midpoint, and the force is applied only in the vertical direction.

3.2 PERFECTLY UNBONDED

We begin by analyzing the system's natural state – the performance of the layered structure while no voltage is applied. In this configuration there are no substantial electroadhesive interactions between the polymer layers; together with our assumption of no mechanical linkages, we therefore treat the entire structure as two disjoint (unbonded) polymer samples with a single force applied (recall the structure of a polymer sample as shown in Figure 2).

For a beam structure consisting of two unbonded layers (assuming minimal shear transfer from polymer contact), an equivalent solution to the elementary deflection equation can be obtained by treating the layers as being side-by-side; in effect, solving the equation for one beam of double width (see Figure 5).

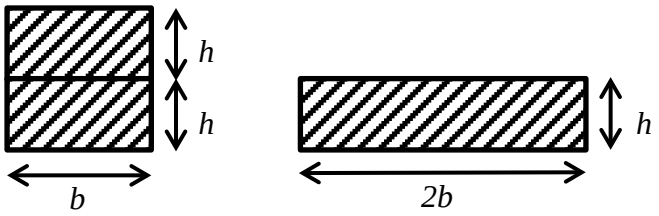

Figure 5. Equivalent geometries for a beam consisting of two unbonded layers.

We recall the formula for the second moment of inertia of a rectangular cross section and the formula for rigidity.

$$I_u = \frac{(2b)h^3}{12} \tag{19}$$

$$EI = \frac{PL^3}{48\delta} \tag{20}$$

From the above equation, we can find the effective rigidity of any layered structure of polymer samples while under no applied voltage. We substitute the dimensions of a polymer sample, as well as the force-deflection pairs given by Ladd. A summary of our results is shown in the tables below.

Table 2. Analytical stiffness and rigidity of unbonded beams under no applied voltage.

Polymer	**Stiffness (N/m)**	**Effective Rigidity (Nm^2)**
PEAA	161	1169
PEAA-TMAH	151	558
PEAA-TEAH	86	339
PEAA-TPAH	62	272

For validation purposes, we compare the modeled values to the results found by Ladd.

Table 3. Comparison of analytical and experimental rigidity under no applied voltage.

Polymer	Analytical Rigidity (Nm^2)	Experimental Rigidity (Nm^2)	Difference
PEAA	1169	1169 ± 51.7	0.00%
PEAA-TMAH	558	530 ± 7.6	5.29%
PEAA-TEAH	339	339 ± 7.4	0.04%
PEAA-TPAH	272	267 ± 8.2	1.97%

With at most approximately five percent variation, we can state with confidence that for the low voltage range, elementary theory closely models the results found by Ladd.

3.3 PERFECTLY BONDED

In this section we treat the structures as unified beams with total dimensions equal to the vertical stack of individual layers. Again, we recall the formula for rigidity and alter the equation of second moment of inertia to reflect our new geometry.

$$I_b = \frac{b(2h)^3}{12} \tag{21}$$

$$EI = \frac{PL^3}{48\delta} \tag{22}$$

The increase in effective rigidity comes about through electroadhesive effects. In general, we observe a fourfold increase in effective rigidity (PEAA excepted). Substituting into our rigidity formula, we find the upper limit of our model; the results are summarized below.

Table 4. Summary of analytically-determined rigidity and moduli in fully-bonding voltage.

Polymer	Stiffness (N/m)	Effective Rigidity (MPa)
PEAA	5171	1039
PEAA-TMAH	19200	1320
PEAA-TEAH	10880	1048
PEAA-TPAH	7680	2180

Unlike the unbonded case, there are no fully-bonded empirical results collected by Ladd to compare our theoretical values against. Instead, Ladd's experimental data shows a gradual increase in rigidity through voltages that fall into the intermediate case; data collection terminates before reaching the upper modulus threshold. Modeling these empirical results forms the focus of the next chapter.

4.0 EMPIRICAL DEVELOPMENT OF INTERMEDIATE CASE

We now turn our attention to characterization of the behavior between the two extremes defined above. From the experimental data, we observe an initially flat regime (the unbonded case), followed by an accelerating rise in rigidity as the increase in J-R effect dominates natural inter-polymer shear. This behavior is consistent with the form of the J-R force, which increases with the square of effective voltage. However, our elementary bending model suggests that after some voltage, there will be no additional increase in rigidity. Intuitively, we might expect that prior to this cutoff point increasing voltage exhibits diminishing returns. This type of saturation behavior is common in physical phenomenon. If this were not the case, we would expect to observe a discontinuous "corner" when the increased rigidity hits its theoretical maximum.

To accommodate the expected behavior of our model, we look to choose a form of equation that varies between an asymptotic minimum and maximum, with a gradual intermediate evolution. For modelling simplicity, we choose a logistic s-curve. The form of such a logistic curve is:

$$f(x) = \frac{L}{1+e^{-C(x-x_0)}} \tag{23}$$

Here, L is the maximum value of the curve, C is a scaling factor that determines the steepness of the slope at the inflection point, and x_0 is the x-value of the midpoint. This form of the equation assumes an initial value of zero. We substitute our variable names and modify the form of the equation to fit to our data by adding an offset corresponding to the zero voltage case modulus.

$$EI(v) = EI_u + \frac{EI_b - EI_u}{1 + e^{-C(v - V_0)}} \quad (24)$$

We are solving for the effective elastic rigidity *EI* at a particular voltage *v*. The rigidity varies between initial unbonded rigidity EI_u and final fully-bonded rigidity EI_b. We assume that the midpoint voltage V_0 depends on the polymer properties, as does the scaling factor *C;* these must be determined so as to fit experimental data, ideally with a physical rationalization. In Figure 6 we show several possible logistic curves to fit example data, and illustrate how midpoint voltage can be estimated by finding the intercept between rigidity and a logistic curve.

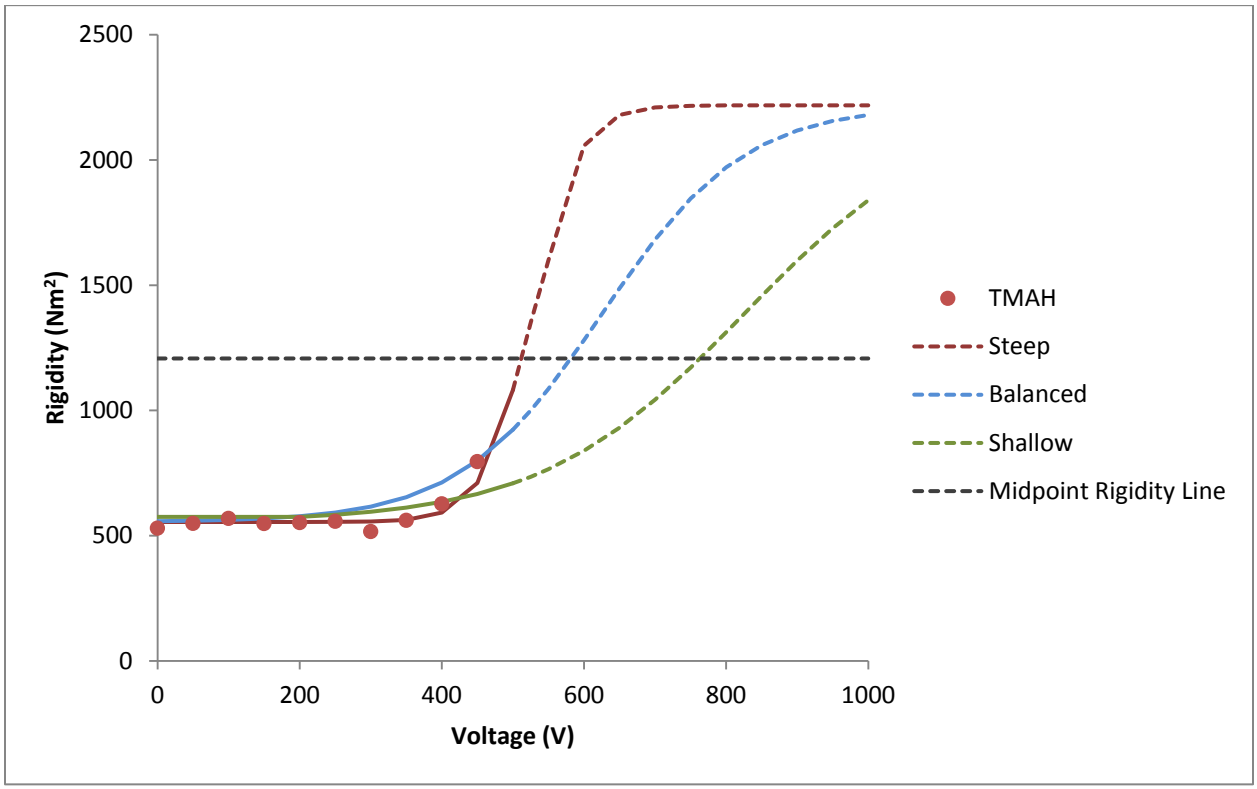

Figure 6. Examples of different logistic fits to experimental data for PEAA-TMAH. While all curves begin and end at the same values, the behavior at intermediate voltages differs greatly. We use a dotted line to represent extrapolation to voltages higher than those measured experimentally. The midpoint voltage can be found by dropping a perpendicular line where each curve intersects the midpoint rigidity line, which represents the halfway point between minimum and maximum rigidity.

As we fit a logistic curve to the existing data, we search for a definition for V_0 and C values that can be applied to all datasets. In the lower range of voltages, we can comfortably fit our curve to experimental data, and we extrapolate the expected behavior for higher voltages. Because of the symmetrical behavior of the logistic curve, we can develop an expression for the full curve from which we can derive our constant values. We discuss the case of each polymer below.

4.1.1 Poly (ethylene-co-acrylic Acid)

Recalling Figure 3, PEAA demonstrated no substantial changes in rigidity across the measure voltage ranges. This is consistent with its status as the control polymer. Similarly, we would expect that in the intermediate voltage case it experiences no change between initial rigidity EI_u and final rigidity EI_b. Therefore, the numerator in our logistic equation collapses to zero, and our solution for the rigidity with respect to voltage is trivial; $EI = EI_u = EI_b$, as expected.

4.1.2 Tetramethylammonium Hydroxide

While all the polymers (PEAA excepted) experience proportionately equivalent increases in rigidity in our model, PEAA-TMAH demonstrates the greatest absolute increase (approximately 220 MPa), due to its larger initial modulus. This is accounted for by our adjustment for non-zero initial values. However, it also exhibits the slowest start to modulus evolution with voltage (an inflection point does not occur until the 350V point) and a shallow curve; as such we expect a later midpoint for a logistic curve.

4.1.3 Tetraethylammonium Hydroxide

PEAA-TEAH experiences a moderate absolute increase in rigidity, falling between the other tested polymer solutions at a 120 MPa increase. While it has the earliest inflection point among tested polymers, the slope of its curve indicates a more intermediate logistic midpoint, suggesting that a hitherto unaccounted-for property governs the value for V_0.

4.1.4 Tetrapropylammonium Hydroxide

At only a 90 MPa increase, PEAA-TPAH shows the lowest absolute increase in rigidity. However, its increase with voltage slopes upwards the most rapidly of any of the tested polymers, despite only having an intermediate inflection point (that is to say, while it is not the first to start increasing, it reaches its ultimate value sooner.) Again, we are lead to believe that the logistic midpoint voltage is unrelated to the inflection voltage, and follows a different trend.

4.1.5 Determination of Constants

We have two available constants to modify in our logistic expression; the inflection voltage V_0 and the scaling factor k must be chosen to coincide with our observations on polymer behavior above. We seek to relate each to a material property or some other physical constant. To do so, we consider the case of V_0. We observe that from TMAH to TEAH to TPAH, the midpoint voltage must steadily decrease; this trend matches the trend in the resistivities ρ of polymers.

To explicitly relate resistivity to midpoint voltage, we estimated the midpoint voltage for each polymer, plotted the estimates as a function of resistivity, and performed a nonlinear

regression to develop an expression. To isolate the effects of altering midpoint voltage, we chose an arbitrary value for *C,* the exponent scaling factor. We then substituted these estimates into our model for rigidity and determined closeness-of-fit for the known low-voltage data collected by Ladd. This process was iterated repeatedly until a satisfactory fit was achieved across all tested polymer solutions. The final model used for relating resistivity to midpoint voltage is shown below; a *C* value of -.01 was used so as to reduce the magnitude of the exponent.

$$V_0 = 483 * \rho^{-.216} \tag{25}$$

4.2 A COMPLETE EMPIRICAL MODEL

Having characterized the three distinct behavioral regions of the polymer and developed expressions for any unknown constants, we can now express our complete model. We choose now to work in terms of the effective modulus of the beam, as opposed to its effective rigidity; while the modulus is not actually being altered, assumption of a uniform modulus throughout the cross section of the beam allows us to calculate an effective modulus and extend the results to rigidity. Recalling the expressions for I_u and I_b (equations 19 and 21 respectively), and equation 25, we can substitute all the values into our logistic s-curve:

$$EI(v) = EI_u + \frac{EI_b - EI_u}{1 + e^{-.01\left(v - \left(483 * \rho^{-.216}\right)\right)}} \tag{26}$$

When we simplify, we can see rigidity *EI* (and by extension, effective modulus) is exclusively related to measureable quantities – the sample dimensions (*b*, *h*, *L*, captured by *I* terms), the applied load (*P*), the resistivity of the polymer (ρ), and the voltage applied to the sample (*v*).

For a final comparison, we applied the above model to each of the polymers tested by Ladd. In Figure 7, we show the predicted modulus from our model alongside the results directly collected by Ladd; we also include a tabular summary in Table 5.

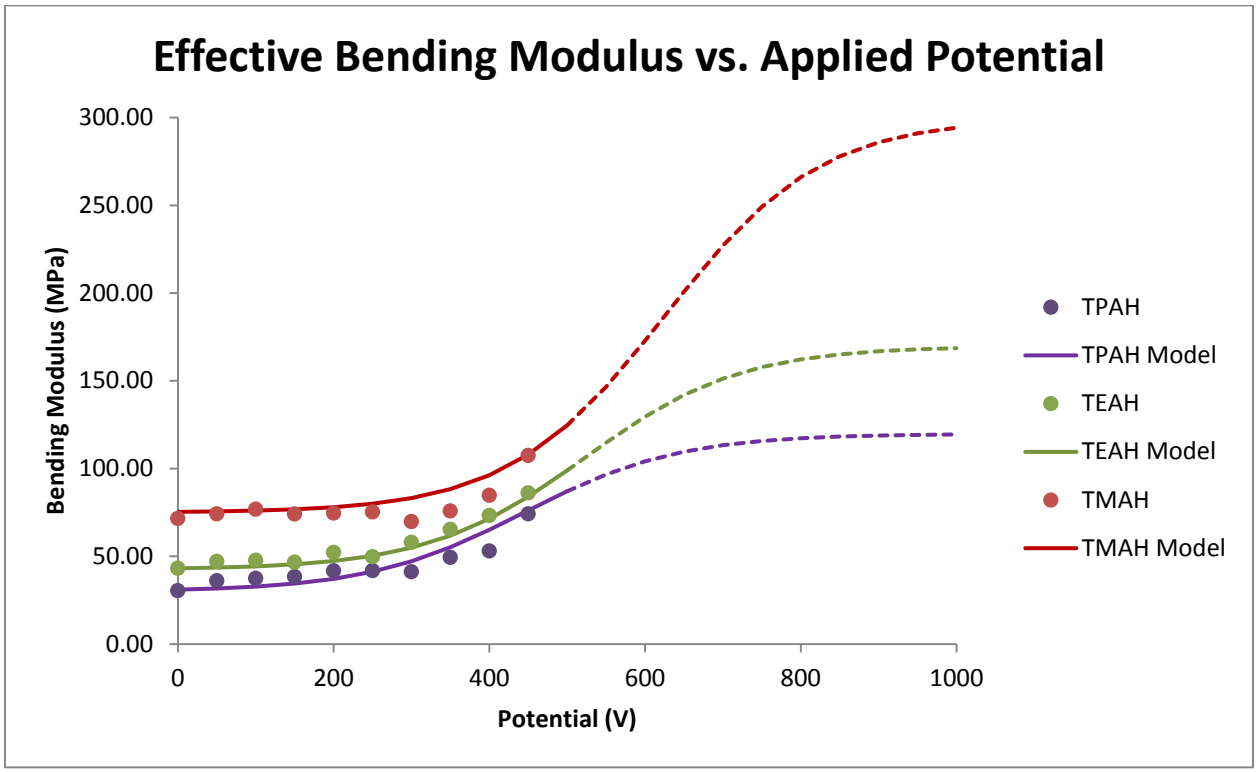

Figure 7. Comparison of modeled and experimental effective bending modulus in polymers demonstrating electroadhesive responses. Dashed lines indicate extrapolation above experimental voltages.

Table 5. Experimental effective modulus versus modelled modulus.

	TPAH Moduli (MPa)		TEAH Moduli (MPa)		TMAH Moduli (MPa)	
Potential (V)	**Experimental**	**Modelled**	**Experimental**	**Modelled**	**Experimental**	**Modelled**
0	30.4	31.0	43.0	43.1	71.5	75.3
50	36.0	31.7	47.0	43.5	74.1	75.6
100	37.4	32.7	47.7	44.3	76.8	76.0
150	38.4	34.4	46.6	45.4	74.0	76.8
200	41.7	37.1	52.2	47.3	74.5	78.0
250	41.8	41.2	49.7	50.3	75.2	80.0
300	41.2	47.1	57.9	54.9	69.7	83.2
350	49.3	55.1	65.3	61.7	75.7	88.3
400	53.0	65.1	73.2	71.4	84.7	96.2
450	74.1	76.1	86.1	84.0	107.4	107.9
500	-	87.1	-	99.0	-	124.6
550	-	96.6	-	114.8	-	146.6
600	-	104.1	-	129.6	-	172.9
650	-	109.6	-	141.9	-	200.8
700	-	113.3	-	151.3	-	227.1
750	-	115.8	-	157.9	-	249.2
800		117.3		162.2		266.0
850		118.3		165.1		277.9
900		118.9		166.9		285.9
950		119.2		168.0		291.0
1000		119.4		168.6		294.3

5.0 SURVEY OF EXTENDED METHODS

While a useful first insight, our analytical-empirical model is simplistic, and lacks substantial theoretical justification. To expand and reinforce our model, we conducted a further review of available literature relating to bending of complex or composite beams, as well as literature relating to adhesion. In particular, we examined the mechanically-bonded composite beams omnipresent in civil engineering, the mechanics of adhesion from both mechanical and electroadhesive sources, and alternative beam-bending theories like Timoshenko and Sandwich theory. A selection of the most promising literature is discussed below; these form the basis of our extended model. While doubtful that any one theory may provide a complete solution, we hope to combine elements of each to more rigorously justify our bending model.

5.1 TIMOSHENKO BEAMS AND SANDWICH BENDING THEORY

The remainder of the thesis focuses on a potential analytical model to capture the intermediate behavior of the electroadhesive bonded beam; that is, when the voltage is greater than zero but less than that which produces a fully-bonded beam. We will develop a method that takes into consideration partial bonding of the layers. An obvious first choice for refining our model in this way is to consider alternatives to elementary bending theory. Our first consideration is

Timoshenko beam theory, which is a generalized version of elementary theory; indeed, if certain conditions are met, the two are equivalent.

5.1.1 Timoshenko Beam Theory

Timoshenko theory was first proposed by Stephen Timoshenko in 1921, and differs from elementary bending theory primarily in its boundary conditions – although there is still zero vertical displacement at the supports, the end faces of beam do not have to remain 'perpendicular;' some rotation relative to the beam's major axis is possible due to shear effects [S. Timoshenko, 1921]. These conditions can be summarized by quantifying the displacement *u* for an arbitrary point with coordinates *x, y, z*.

$$u_x = -z\varphi(x) \tag{27.1}$$

$$u_y = w(x) \tag{27.2}$$

$$u_z = 0 \tag{27.3}$$

Here φ is the angle of rotation of the end face of the beam relative to the z-axis, and *w* is the displacement of the beam's midpoint along the z-axis (roughly analogous to deflection δ from our earlier derivation of elementary theory). For a beam satisfying these displacement conditions, we can apply the system of uncoupled differential equations outlined below.

$$\frac{d^2}{dx^2}\left(EI\frac{d\varphi}{dx}\right) = P(x,t) \tag{28}$$

$$\frac{dw}{dx} = \varphi - \frac{1}{\kappa bhG}\frac{d}{dx}\left(EI\frac{d\varphi}{dx}\right) \tag{29}$$

In contrast to elementary theory, our solution here depends on the shear modulus *G* and the Timoshenko shear constant κ, which is governed by geometry and Poisson's ratio. For most rectangular cross sections, the shear constant is approximately 5/6 (we recall that a general

rectangular beam has width b and height h). Furthermore, we note that determining a solution for this system demands boundary conditions; since our beam is simply supported, we can draw our conditions from the displacement at the supports, $w = 0$ for $x = 0$ and L.

While applying Timoshenko beam conditions provides a more generalizable result than elementary bending theory, for certain types of beams they produce nearly indistinguishable results. The following inequality provides a simple test to determine if the theories produce equivalent results; if it is satisfied, either theory can be used.

$$\frac{EI}{\kappa b h L^2 G} \ll 1 \tag{30}$$

For our purposes, while incorporating Timoshenko bending conditions across the entire voltage spectrum might provide more accurate results overall, it is of particular interest at the upper end of the voltage curve, where the polymer layers are mostly bonded together. This is because Timoshenko beams can be utilized in sandwich theory.

5.1.2 Sandwich Theory

Sandwich bending theory applies to a certain class of structure with thin, rigid face plates and a comparatively flexible inner layer (see Figure 8). The thickness f of each face plate is considered to be much smaller than the total thickness of the inner layer, $2h$. This is analogous to our layered structure –an inner core layer of deformable polymer is enclosed by comparatively stiff but thin outer electrodes. Because the archetypical sandwich beam only contains one core layer, however, we would expect to be limited to modelling the upper range of voltages, where the adhesive forces cause the polymers to behave as a single layer. In other words, while at a

given voltage full bonding may not necessarily have been achieved, to make use of sandwich theory we assume it has, and treat the polymer layers a single layer.

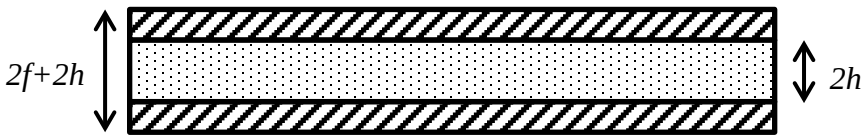

Figure 8. Simple representation of a sandwich beam

Modelling the behavior of a sandwich beam is typically undertaken using a combination of bending theories. The thin, rigid faceplates are commonly modelled as governed by elementary bending theory assumptions, while the inner layer uses either the same assumptions as elementary bending theory, or those that govern Timoshenko beams [D. Zenkert, 1995]. In its most general form, for a beam satisfying the sandwich geometry, sandwich beam behavior is modelled according to the following system of equations for rigidity *K* and shear stiffness *S*:

$$K_{comp} = \frac{f(2h+f)^2}{2}\frac{\sigma_{face,x}}{\varepsilon_{face,x}} \tag{31}$$

$$K_{face} = \frac{f^3}{12}\frac{\sigma_{face,x}}{\varepsilon_{face,x}} \tag{32}$$

$$S_{comp} = S_{inner} = \frac{\kappa(2h+f)}{2}\frac{\tau_{inner,zx}}{\gamma_{inner,zx}} \tag{33}$$

Here again we incorporate normal (ε) and shear (γ) strain, as well as normal (σ) and shear (τ) stress. We use the subscript *comp* to refer to the composite beam (both face plates and inner layer). Note that the shear constant term κ is not necessarily equivalent to the Timoshenko shear constant. Furthermore, while in Timoshenko theory we dealt with a single displacement *w*, in sandwich theory we differentiate between displacement resulting from bending, w_b, and displacement from shear, w_s.

The three above equations can be reconfigured to generate a system of two governing differential equations for bending moment *M* and shear force *V*:

$$M = K_{comp}\frac{d^2w_s}{dx^2} - \left(K_{comp} + 2K_{face}\right)\frac{d^2w}{dx^2} \tag{34}$$

$$V = S_{inner}\frac{dw_s}{dx} - 2K_{face}\frac{d^3w}{dx^3} \tag{35}$$

In conjunction with boundary conditions on the deflection at the supports, and knowledge of the applied load, this system of equations can be solved. If we choose to neglect Timoshenko theory and treat both the face plates and the inner layer with elementary theory instead, a simplified solution presents itself:

$$\sigma_{face,x} = \frac{M}{2fh} \tag{36.1}$$

$$\sigma_{inner,x} = 0 \tag{36.2}$$

$$\tau_{face,zx} = 0 \tag{36.3}$$

$$\tau_{inner,zx} = \frac{Q}{2h} \tag{36.4}$$

In other words, in an elementary-bending-only regime, the stresses in the face plates are only affected by the moment in the beam, while the stresses in the core are only affected by the shear force. When taken with the assumption that the face plates dominate the inner layer in both thinness ($f < 2h$) and rigidity ($E_{face} > E_{inner}$), we can then conclude that rigidity for the entire beam takes the following form:

$$K_{comp} = 2E_{face}fh(f + h) \tag{37}$$

From an effective rigidity, finding the effective modulus becomes a trivial exercise. If we make the reasonable assumption that our polymer structure satisfies the thin and rigid criteria, then this provides a compact and useful result that provides a simple way to calculate the effective modulus for the entire beam. However, it falls short of providing a physical justification for the observed behavior, and its usefulness is limited to the upper voltage range, where the assumption that the polymer layers behave as a single unit is less problematic.

5.1.3 A Composite Beam Incorporating Sandwich Theory

As mentioned above, our goal is to capture the intermediate electroadhesive behavior of the beam by considering partial bonding of the layers. We do so by creating composite beam models using sandwich theory. In this section we will develop the general model, and in later sections we will associate it to the electroadhesive beam through the experimental results.

Because the archetypical sandwich beam consists of one core layer with rigid faceplates, we would expect that in a partially-bonded, intermediate-voltage domain state, our sample structure must be represented by some combination of sandwich and 'ordinary' composite beams (a "composite-of-composites" beam, so to speak). We anticipate that a variable area of the beam behaves as a single-core sandwich, representing the fully bonded state, while the unbonded areas continue to behave as an ordinary stack of beams, subject to elementary theory. This representation entails a question of geometry, however: do we represent the 'sandwich domain' along minor or major axis? That is to say, does the area of full bonding appear along the entire width of the beam but only part of the length, along part of the width but the entire length, or some combination therein (see Figure 9)?

Figure 9. Side and end views of a sandwich-composite beam with the sandwich domain running widthwise (a) and lengthwise (b).

5.1.3.1 A Widthwise Sandwich Composite

We can calculate an effective stiffness and modulus for each of these beam geometries for validation against our earlier results, beginning with the widthwise orientation in figure 8(a). In this orientation, the beam has three distinct cross sections along its length; we denote the

length of the sandwich section as *s*. The sandwich section is assumed to occupy the center of the beam, to maintain symmetry. Figure 10 shows such a beam undergoing simply-supported three-point bending.

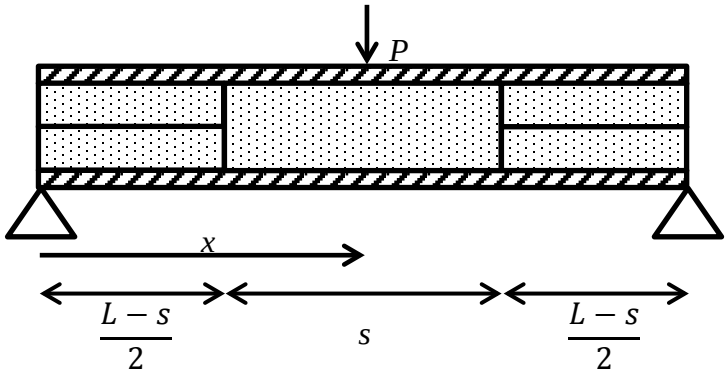

Figure 10. A widthwise sandwich beam of length *L* subjected to a midpoint load *P*.

Solving for the behavior of this beam requires considering each interval; we begin by determining our know quantities and boundary conditions. At the locations of the supports, $x = 0$ and $x = L$, we know that the deflection y must be 0. We also know that due to the symmetry in the beam, each support exerts a reaction force $\frac{P}{2}$ equal to half the force applied at the midpoint. The maximum deflection $y = \delta$ will occur at the midpoint of the beam $x = \frac{L}{2}$. Furthermore, for continuity within the beam, the deflection and slope (y and $\frac{dy}{dx}$) must be consistent at the transitions between intervals ($x = \frac{L-s}{2}$ and $x = \frac{L+s}{2}$).

Next, we define the moment within each interval with respect to x. In the first (leftmost) interval $0 \leq x \leq \frac{L-s}{2}$, there is no reaction moment from the simple support, so the moment increases with x linearly, $M_1 = \frac{P}{2}x$. By a similar token, the third (rightmost) interval also has no reaction moment, causing a linear decrease, $M_3 = \frac{P}{2}(L - x)$. Finally, in the second (middle)

interval, the moment varies between M_1 and M_3, leading to $M_2 = \frac{P}{s}(x - \left(\frac{L-s}{2}\right))$. With all three moments defined, we can use the following differential relationship to relate modulus, deflection, and moment within each segment *n*.

$$E_n \frac{d^2y}{dx^2} = M_n \tag{38}$$

The resulting form for each beam segment is shown below. This system of equations must be successively integrated and solved using our known boundary conditions.

$$E_1 \frac{d^2y}{dx^2} = M_1 = \frac{P}{2}x \tag{39.1}$$

$$E_2 \frac{d^2y}{dx^2} = M_2 = \frac{P}{s}\left(x - \left(\frac{L-s}{2}\right)\right) \tag{39.2}$$

$$E_3 \frac{d^2y}{dx^2} = M_3 = \frac{P}{2}(L - x) \tag{39.3}$$

After integrating once and applying our midpoint boundary condition, we arrive at the following relationships for the slope of the beam:

$$E_1 \frac{dy}{dx} = \frac{P}{4}x^2 + C_{11} \tag{40.1}$$

$$E_2 \frac{dy}{dx} = \frac{P}{2s}x^2 - \frac{P(L-s)}{2s}x - \frac{PL}{4s}\left(\frac{2s-L}{2}\right) \tag{40.2}$$

$$E_3 \frac{dy}{dx} = -\frac{P}{4}x^2 + \frac{PL}{2}x + C_{31} \tag{40.3}$$

Here we must apply our boundary conditions for the interfaces between sections. Equations 40.1 and 40.2 must yield the same result for $\frac{dy}{dx}$ at $x = \left(\frac{L-s}{2}\right)$, and equations 40.2 and 40.3 must yield the same result for $\frac{dy}{dx}$ at $x = \left(\frac{L+s}{2}\right)$. Accordingly, we find that:

$$C_{11} = 2PE_1(8L - s) - E_2(PL^2 - 2PLs + s^2) \tag{41.1}$$

$$C_{31} = \frac{P}{16}(6sE_3 - (3L^2 + 2Ls - s^2)E_2) \tag{41.1}$$

Now we can assemble complete forms of equation system 40, and integrate again to find expressions for the deflection in each beam segment:

$$E_1 y = \frac{P}{12}x^3 + \left(2PE_1(8L - s) - E_2(PL^2 - 2PLs + s^2)\right)x + C_{12} \quad (42.1)$$

$$E_2 y = \frac{P}{6s}x^3 - \frac{P(L-s)}{4s}x^2 - \frac{PL}{4s}\left(\frac{2s-L}{2}\right)x + C_{22} \quad (42.2)$$

$$E_3 y = -\frac{P}{12}x^3 + \frac{PL}{4}x^2 + \left(\frac{P}{16}(6sE_3 - (3L^2 + 2Ls - s^2)E_2)\right)x + C_{32} \quad (42.3)$$

With the equations in this form, we can apply our boundary conditions on deflection at the simple supports and interfaces. We know that $y = 0$ at $x = 0$ and $x = L$, allowing us to solve directly for C_{12} and C_{32}.

$$C_{12} = 0 \quad (43.1)$$

$$C_{32} = -(-9PL^3 - 6sPL^2 + 3s^2PL)E_2 - (18sPL)E_3 - 8PL^3 \quad (43.1)$$

Since the beam must remain continuous, we know that two adjacent segments must have the same deflection y at the interface, allowing us to solve for C_{22}.

$$C_{22} = \frac{1}{96}\Big(\big((1 - 48E_2)PL^3 + \big((96E_2 - 3)s + 768E_1\big)PL^2 - 864E_1PLs + (3PL -$$

$$48(1 + P)LE_2 + 96PE_1)s^2 + (48E_2 - P)s^3\Big)sE_2 - 2(PL^3 - 3PL^2s + 2Ps^3)E_1\Big) \quad (44)$$

While this makes for a tedious substitution, we are now able to express the deflection within each beam segment as a function of the beam dimensions, applied load, and modulus of the constituent segments.

5.1.3.2 A Lengthwise Sandwich Composite

We now consider the alternative orientation of the sandwich beam component; namely, the lengthwise orientation shown in Figure 8(b). Because the beam now maintains the same cross-sectional parameters over its entire length, the problem is more easily tractable.

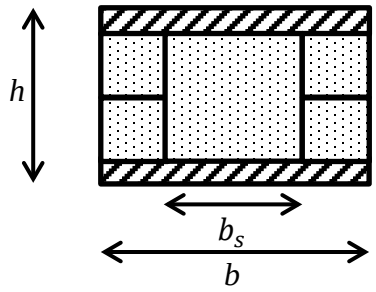

Figure 11. Cross section of a lengthwise sandwich beam.

The cross section of Figure 8(b), shown in more detail in Figure 11. Cross section of a lengthwise sandwich beam.Figure 11, can be broken into three component areas. Occupying the center of the cross section is sandwich layer of width b_s; this includes a fully-bonded section of polymer and the electrode faceplates. On either side of this central area are two areas where the polymer samples remain unbonded, behaving like an ordinary stack of beams. Suppose we were to divide the beam into three pieces based on these cross-sectional areas; we have already discussed how each section behaves during bending above. We recall that our initial analysis of elementary bending theory addressed the bending of the unbonded beams on the edges, while sandwich theory provides a solution for the bending of the middle section. This orientation, then, is equivalent to solving for the three beams side-by-side, which must deflect together as a force is applied (see Figure 12). This is the premise of our analysis for this orientation.

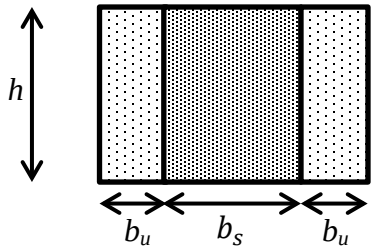

Figure 12. A simplified cross section for a composite beam with three different areas.

Consider the simplified cross section of the beam shown in above. We know the rigidity, and by extension the effective modulus, of the darker central area from sandwich theory. We also know the rigidity and effective modulus of the lighter areas, from the work performed by Ladd. With the rigidity and the dimensions of each section, we can calculate a new, equivalent cross section, allowing us to find the rigidity of the entire beam when subjected to bending. This is known as the transformed section method [Ugural & Fenster, 2003].

To use the transformed section method in a beam of two materials, we must convert the area of one material into an equivalent amount of the other material. For our purposes, we will refer to the sandwich component as being of material "S," and the unbonded components as being of material "U." Currently, there are two areas of material U, each with a height of *h* and width b_u. To preserve bending behavior, we can only alter the width of the new section; the height must remain the same. Converting a width of material U to a new width of material S is a simple ratio of moduli:

$$\frac{E_U}{E_S} b_u = b_{new} \tag{45}$$

If a material with a lower modulus is being converted to a material of greater modulus, the equivalent dimension will be smaller than the initial dimension. In our case, this results in a transformed cross section like the one shown below.

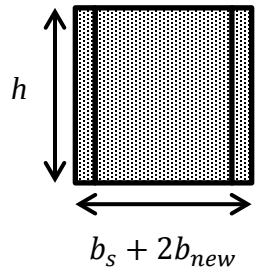

Figure 13. An equivalent cross section based on the transformed section method.

The unbonded beam sections of material U have been replaced; now our beam possesses a completely uniform cross section made entire of material S (modulus E_S), with new dimensions h and b_s+2b_{new}. We can now calculate the new second moment of inertia I, and solve for the bending of the beam.

$$I = \frac{(b_s+2b_{new})h^3}{12} \tag{46}$$

The rigidity of the beam is now the product of E_s and the new value of I. Since the bending of the beam depends on the relationship between the original material widths b_u and b_s, it stands to reason that changes in bending behavior can be caused by varying the size of our sandwich component. Characterizing the bending of the beam then becomes a matter of choosing the dimensions of the sandwich; in later sections, we present a systematic approach for varying the size of the sandwich to match our experimental results.

5.2 AN ANALOGY TO COMPOSITE STRUCTURES

In comparison to composite beams formed by electroadhesion, mechanically-bonded composite beams are a well-studied phenomenon. Let us consider two beams joined by some sort of discrete physical connector, e.g. concrete beams with steel reinforcements. In such a beam, the rigid connections serve to mitigate shear and slip effects during bending. In the process, the material around connectors can become areas of shear concentration; this depends largely on the type of bending (positive versus negative) and the overall geometry of the beam and connections [Fabbrocino *et al.,* 2000]. Established guidelines for civil engineers restrict the size, number, and spacing of shear connectors in structural use depending on the application [Eurocode, 2004][ISO, 2013].

To maintain consistency between engineering bending theory and real-world shear/slip effects, composite structural beam problems can be recast using effective dimensions, rather than the true dimensions. The choice of effective dimensions is dependent on loading and boundary conditions, beam geometry, and the degree of shear connection (roughly equivalent to the ratio of connectors used to connectors needed for zero slip); again, regulatory bodies provide standards for engineering use. For a beam of uniform cross section undergoing a normal force, the primary dimensions of interest are the effective length and width of the beam, as these govern the interfacial area. As a general rule, the effective interfacial area contributing to bending is equivalent to the sum of the areas in close proximity to shear connectors [S. Hicks, 2003].

Assuming that the beams being joined have the same width at the interface, we can further simplify matters by only considering effective length. In other words, if two beams are joined by shear connectors, the bending behavior will depend on the amount of axial length at the interface that is "directly" joined together, rather than the total length of the beams (see Figure 14).

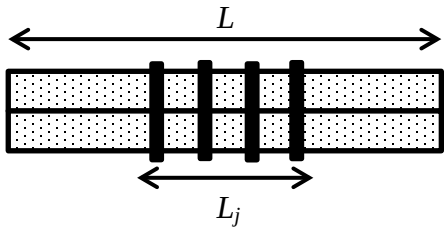

Figure 14. A comparison of total beam length L versus the joined length L_j. Joined length accounts only for the areas of the beam connected by shear connectors (shown here as vertical bars).

The joined length governs the interfacial area contributing to slip and shear effects, which themselves affect the overall bending. We are considering this to be an analogy to the J-R effect on the behavior of our polymer structure.

5.2.1 Approximating Connectors with a Probabilistic J-R Model

Suppose we have two layers of polymer which are not yet joined into a single structure. The surface of any given layer will have a certain roughness. No surface is truly uniform; the number and intensity of micro- (or smaller) scale peaks and valleys contributes towards the roughness parameter. When the two layers are put face-to-face in preparation for joining, the actual distance between the layers will vary continuously over the surface, but can broadly be classified into three kinds of resulting areas – areas where peaks meet, areas where peaks coincide with valleys, and areas where valleys meet. These areas broadly correspond to small, modest, and large distances between the layers, respectively (see Figure 15).

Figure 15. Exaggerated example of surface roughness at the interface between two samples (black areas) and the resulting variations in interfacial distance *g*.

Our interest lies in the areas where valleys meet. This is due to the method by which the J-R effect manifests itself; small gaps between contact areas result in electroadhesive force, with smaller gaps creating greater force. By establishing some cutoff gap size that distinguishes between weak and strong J-R effects, we can choose to treat the areas of maximal attractive force as discrete points of connection, analogous to the shear connectors discussed above. We propose that by approximating the quantity of these discrete points of connection according to the surface roughness of the polymer, we can determine the percentage of total interfacial area contributing to stiffness using the civil engineering principles outlined above. Once we have a figure for effective area, calculating an effective stiffness becomes an exercise in implementing the calculations discussed in previous sections. While either the widthwise or lengthwise approach

could be used, the most accurate results would depend on a combination of the two, a substantially more difficult calculation. For our purposes, we will focus our later analysis on the lengthwise approach.

5.2.2 A Simple Simulation for Determining J-R Contributing Area

In order to estimate the amount of J-R contributing area at the interface of two samples, we created a basic program to generate and pair of random polymer surfaces and calculate the proportion of interfacial distance above an arbitrary threshold. The random surfaces are created using a probabilistic model for surface roughness, parameterized using both maximum height variation and average peak-to-peak distance to generate surfaces. While randomized approaches to polymer surface roughness have been previously explored, previous studies have been more motivated by material science concerns [J. Douglas, 1989]; the exploration centers on the specific structures of the polymers, the resulting geometries and properties, etc. In our case, a more simplistic approach is warranted. A sample is divided into a number of cells that varies based on sample dimension and average peak-to-peak distance (to reduce computational complexity).

After generating 3000 sample surfaces for any given roughness criteria, the samples are paired at random. Matched samples are positioned face-to-face such that the minimum possible interfacial distance is zero, at which point the mean interfacial distance is calculated. For each pair of overlapping cells, the interfacial distance is compared to the mean value. Because the J-R effect is more pronounced in smaller gap sizes, cell pairs with “large” interfacial distances do not contribute to the effective area, while cell pairs with “small” distances do; the total contributing

area is the sum of the areas of cell pairs with small interfacial distances. The total contributing area is then taken as a proportion of total sample surface area.

Because the distinction between large and small interfacial distances is arbitrary, we establish cutoff points expressed in 5% increments of the mean interfacial distance. In other words, we pick a cutoff point corresponding to some proportion of the mean interfacial distance; any gap smaller than the cutoff point contributes to the effective area. If we assume that the interfacial distance will be normally distributed, then in theory a 200% cutoff threshold (e.g. any gap, no matter the size) will represent the full area of the beam contributing. 100% cutoff threshold (e.g. any gap smaller than the mean) should result in half of the area contributing to stiffness, and a 0% threshold (e.g. only areas of direct contact) should result in nearly zero area contributing. We note that our definitions of contributing area and gap size should not be confused with the effective contact area term in Equation (2) for determining J-R force; rather than try to quantify the J-R forces directly, we are more interested in the areas being affected. The table below summarizes the results for a sample matching those prepared by Ladd (19.0 mm x 25.4 mm interface dimensions for a total surface area of 482.6 mm^2).

Table 6. Proportion of area contributing to stiffness depending on threshold of J-R effect.

J-R Threshold (%)	Contributing Area (mm^2)	Contributing Area (%)
200%	481.63	99.80%
195%	481.63	99.80%
190%	481.63	99.80%
185%	476.33	98.70%
180%	471.98	97.80%
175%	466.67	96.70%
170%	459.92	95.30%
165%	451.23	93.50%
160%	443.03	91.80%
155%	432.89	89.70%
150%	421.31	87.30%
145%	408.76	84.70%
140%	394.77	81.80%
135%	379.81	78.70%
130%	363.40	75.30%
125%	345.54	71.60%
120%	327.20	67.80%
115%	307.42	63.70%
110%	286.66	59.40%
105%	263.98	54.70%
100%	240.91	49.9%
95%	217.75	45.1%
90%	195.40	40.5%
85%	174.41	36.1%
80%	154.34	32.0%
75%	135.85	28.2%
70%	118.19	24.5%
65%	102.02	21.1%
60%	86.82	18.0%
55%	72.92	15.1%
50%	60.33	12.5%
45%	48.84	10.1%
40%	38.51	8.0%
35%	29.54	6.1%
30%	21.67	4.5%
25%	15.15	3.1%
20%	9.70	2.0%
15%	5.45	1.1%
10%	2.41	0.5%
5%	0.62	0.1%
0%	0.14	0.00%

We observe that our simulated contributing areas follow a normal distribution, as anticipated. These derived areas can now be substituted into a new estimate for effective rigidity; when taken in conjunction with the sandwich theory approach in Figure 9, these values could serve as the basis for determining the dimension of the sandwich beam component. In other words, when in reality disjoint contributing areas are uniformly distributed across the interface, we make the assumption that we can concentrate the contributing area into a fully bonded lengthwise strip (as depicted in Fig. 8b) of equivalent area. In this case, at a 200% J-R threshold, the entire surface area is contributing to the J-R effect, and the sandwich component of the beam will occupy the full size of the beam. Conversely, a 0% J-R threshold indicates that no area contributes to the J-R effect, so there is no sandwich component to the beam. The selection of J-R threshold will be dependent on both the choice of polymer and on the voltage applied to the beam, with higher voltages presumably causing greater thresholds. In this way, we can tie contributing area to voltage for each polymer.

5.2.3 Applying J-R Contributing Area to an Effective Modulus Calculation

Let us consider a test case of the above theory, i.e. using an estimated J-R contributing area as the size of the sandwich component in a composite-of-composites beam. We assume that the sandwich component is located in the center of the beam (as shown in Figure 9b). Supposing we use the same dimensions for our polymer samples as those used by Ladd (19 mm x 25.4 mm at the interface), we can find the sandwich dimensions at different J-R area contributions. In the most trivial case, a 0% area contribution leads to no sandwich component, and the problem is reduced to the elementary beam bending solution for unbonded beams. The sandwich section becomes increasingly dominant as the J-R contributing area increases; in our transformed beam,

it accounts for an increasingly large portion of the effective cross section. Recalling our discussion of sandwich beams, we note that the rigidity of each polymer (or more specifically, the ratio of the fully-bonded rigidity to the unbonded rigidity) will also play a role in deciding the relative size of the sandwich component of the transformed beam. For this reason, we note in Table 7 that each polymer shows a different width b_s value for a given area contribution. Our focus is on the lengthwise orientation; the table below summarizes the relative dimensions of the sandwich component at each J-R contributing area value.

Table 7. Summary of J-R dependent dimensions for a lengthwise sandwich component, expressed as a percentage of the area of the transformed beam.

	Lengthwise Sandwich			
J-R Contributing Area (%)	**Width b_s (%)**			
-	PEAA	TMAH	TEAH	TPAH
99.80%	99.8%	100%	99.9%	99.9%
98.70%	98.5%	99.7%	99.7%	99.7%
97.80%	97.5%	99.5%	99.4%	99.4%
96.70%	96.3%	99.2%	99.1%	99.1%
95.30%	94.7%	98.8%	98.8%	98.8%
93.50%	92.7%	98.3%	98.3%	98.3%
91.80%	90.9%	97.9%	97.8%	97.8%
89.70%	88.6%	97.3%	97.1%	97.2%
87.30%	85.9%	96.6%	96.4%	96.4%
84.70%	83.1%	95.8%	95.6%	95.6%
81.80%	80.0%	94.9%	94.6%	94.6%
78.70%	76.7%	93.8%	93.5%	93.6%
75.30%	73.0%	92.6%	92.3%	92.3%
71.60%	69.1%	91.2%	90.8%	90.8%
67.80%	65.2%	89.7%	89.2%	89.2%
63.70%	60.9%	87.8%	87.3%	87.3%
59.40%	56.5%	85.8%	85.1%	85.2%
54.70%	51.8%	83.2%	82.5%	82.6%
49.9%	47.0%	80.4%	79.6%	79.7%
45.1%	42.2%	77.2%	76.3%	76.4%
40.5%	37.6%	73.6%	72.6%	72.7%
36.1%	33.4%	69.9%	68.9%	68.9%
32.0%	29.5%	65.9%	64.8%	64.9%
28.2%	25.9%	61.8%	60.6%	60.7%
24.5%	22.4%	57.2%	55.9%	56.0%
21.1%	19.2%	52.4%	51.1%	51.2%
18.0%	16.3%	47.5%	46.2%	46.3%
15.1%	13.7%	42.3%	41.0%	41.1%
12.5%	11.3%	37.0%	35.9%	36.0%
10.1%	9.1%	31.6%	30.5%	30.6%
8.0%	7.2%	26.4%	25.4%	25.5%
6.1%	5.6%	21.7%	20.8%	20.9%
4.5%	4.0%	16.2%	15.6%	15.6%
3.1%	2.8%	11.6%	11.1%	11.2%
2.0%	1.8%	7.7%	7.4%	7.4%
1.1%	1.0%	4.4%	4.2%	4.2%
0.5%	0.4%	2.0%	1.9%	1.9%
0.1%	0.0%	0.0%	0.0%	0.0%
0.00%	0.0%	0.0%	0.0%	0.0%

Now we can use these dimensions, together with the results found in Section 5.1, to calculate the deflection in a sample. We have access to all the dimensions of the sample; we know from Ladd's work and our elementary theory approach the effective modulus of unjoined layers; elementary and sandwich theories give us two alternatives for the modulus of the fully-bonded component. Furthermore, we can use these results to compare the rigidity of a hypothetical beam at different J-R contributing area values to the experimental results collected by Ladd. For the purposes of simplicity, we will focus our discussion on the lengthwise orientation; however, this approach should be equally valid for a properly-defined widthwise component.

Recalling our solution to the bending of a lengthwise sandwich beam, we note that the J-R contributing area for the lengthwise sandwich is representative of the ratio of b_s and b_u. This allows us to find the second moment of inertia for the composite beam, which we can use to find rigidity. This modelled rigidity can then be related to an experimental rigidity at a given voltage, allowing us to relate J-R contributing area and voltage. Below we present our modelled rigidity, and draw comparisons with the experimental data (repeated from above).

Table 8. Modelled rigidity results at various J-R area contributions, assuming a lengthwise bonded beam over areas defined in Table 7. We highlight each column in such a way as to reflect those points with similarity to experimental data.

	Modelled Rigidity (Nm^2)			
J-R Contributing Area (%)	**PEAA**	**TMAH**	**TEAH**	**TPAH**
0.00%	1169	530	339	267
0.50%	1169	530	339	267
1.10%	1168	538	344	271
2.00%	1168	548	350	275
3.10%	1166	563	359	282
4.50%	1165	581	370	291
6.30%	1163	604	384	302
8.00%	1161	634	402	316
10.10%	1159	662	418	329
12.50%	1156	696	439	346
15.10%	1153	736	463	364
18.00%	1149	779	489	385
21.10%	1146	827	517	407
24.50%	1142	878	548	431
28.20%	1137	934	581	458
32.00%	1132	995	618	487
36.10%	1127	1058	656	517
40.40%	1122	1125	696	549
45.10%	1117	1196	739	582
49.90%	1110	1274	785	619
54.70%	1104	1353	833	656
59.40%	1098	1432	880	694
63.70%	1092	1510	926	731
67.80%	1086	1581	969	764
71.60%	1081	1649	1010	796
75.30%	1076	1711	1047	826
78.70%	1071	1772	1084	855
81.80%	1067	1828	1117	881
84.70%	1063	1880	1148	906
87.30%	1059	1927	1177	928
89.70%	1056	1970	1202	949
91.80%	1052	2010	1226	967
93.50%	1050	2045	1247	984
95.30%	1047	2073	1264	997
96.70%	1045	2102	1281	1011
97.80%	1043	2125	1295	1022
98.70%	1042	2144	1306	1031
99.80%	1041	2158	1315	1038

Table 9. Condensed experimental results from Ladd, repeated for clarity. See also Table **1**.

	Experimental Effective Rigidity (Nm^2)			
Applied Potential (V)	**PEAA**	**TMAH**	**TEAH**	**TPAH**
0	1169.0	529.8	339.3	266.6
50	1130.0	549.1	370.4	316.1
100	1117.2	568.7	375.8	328.4
150	1085.8	548.3	367.1	337.1
200	1090.2	552.2	411.0	365.3
250	1111.0	557.3	391.2	366.3
300	1112.0	516.5	456.1	361.1
350	1045.4	561.0	514.4	432.7
400	1069.8	627.2	576.2	464.6
450	1039.0	795.4	677.8	650.3

When we compare the modelled results (Table 8) to the experimental rigidity results obtained by Ladd (Table 9), we can immediately draw comparisons. At a 0% area contribution, our model matches the experimental results for all polymers under the zero-voltage condition. This makes sense, as at 0V there are no J-R effects manifested. As the J-R contributing area increases, we observe that the rigidity increases, as expected. At the maximum area contribution case, our modelled rigidities nearly align with those predicted by elementary modelling. Figure 16 shows multi-axis plots comparing rigidity versus threshold and voltage for each non-control polymer. In each plot, the modelled data is drawn from Table 8, while the experimental results are drawn from Table 9.

To position the data, we pin 100% J-R area contribution (the maximum of the axis) to the voltage required to raise rigidity to within 1% of the maximum value suggested by our empirical model. Then, we scale the lower bound of the axis by pinning 0% area contribution to the voltage where the rise in rigidity begins – a rough metric we define as the last experimental data point showing an increase of less than 10% on the preceding value. This gives us a consistent approach to find a fit between modelled curve and experimental data. However, because of our criteria for the location of the 0% area contribution, we would need to express negative

percentages of area to fully cover the experimental data range. Consider TMAH as an example. While the best match between the model and experimental data puts the 0% area contribution at around 350V, it stands to reason that if there is no J-R beam bonding at that voltage, there would be no bonding at lower voltages either. However, if 0% area coincides with 350V, then in order to model 0V, we would need a contributing area of -60%. This is physically meaningless; since "no J-R bonded area" is the least-possible bonding condition, contributing areas with values less than 0% would indicate that until a critical voltage is reached, some source of adhesion other than J-R effect is dominant. To accommodate this, we instead extend the 0% area contribution condition downwards to 0 voltage, the "true" unbonded state. Then, we restart the area contribution percentage at a new value which we adjust to achieve a good fit between axes. This realignment shifts the contributing area needed to produce a given rigidity, which would indicate some other bonding force beyond the J-R effect. An obvious candidate for this force could be the innate shear between polymer layers caused by friction, which would logically vary depending on the "stickiness" of each polymer. In this way, each polymer would have some innate range of contributing area at which no substantial J-R effects manifest.

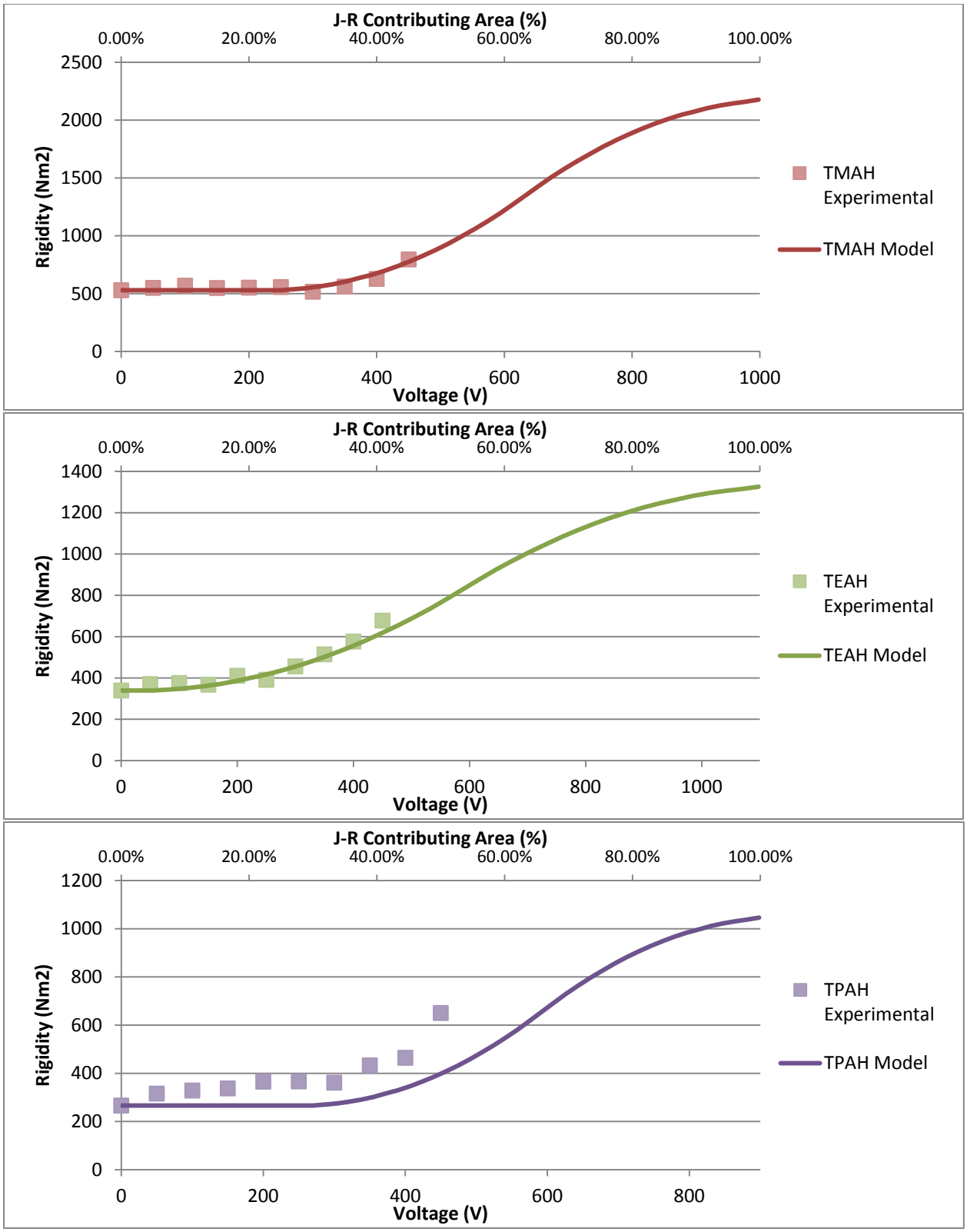

Figure 16. Comparison plots showing the relationship between contributing area and applied voltage for a given rigidity, separated by polymer.

We observe that for all polymers, the contributing model can be positioned to match the experimental data, with varying degrees of success. Each polymer relates contributing area to applied voltage differently; we use adjusted starting area contributions of 25% for TMAH, 5% for TEAH, and 30% for TPAH. Assuming these values are governed by the innate friction within the polymers, our results match the trends found in previous research, which showed TPAH to have the highest self-adhesion. However, we note that our modelled rigidities for TPAH fall short of the experimental data, possibly due to the outlier status of the 0V experimental rigidity. Additionally, modelled rigidities exceed those measured experimentally; no experimental data collected at 450V exceeds a 50% area contribution value. If we assume our model reflects the behavior of the real system, the question then becomes one of how to achieve higher ratios of bonded area. The obvious solution is to increase the applied voltage – we observe from the data that 800-1000V would correspond to a 100% threshold. However, due to concerns with sample arcing, increasing the voltage has a practical limit and fails to address the underlying question. A more fundamental approach would be to modify the polymers themselves; altering the properties in such a way as to increase the rate the bonding increases with voltage.

Finally, while the agreement between modelled and experimental data would suggest that our model is based on sound principles, further understanding of the relationship between J-R contributing area and voltage evolution must be developed. It is entirely possible that neither the elementary bending model nor the threshold model accurately capture the full behavior of the polymers.

5.3 AN ADHESION PERSPECTIVE

We now turn our consideration towards the study of ordinary adhesion mechanics in literature. While our primary interest lies in understanding electroadhesion, there are useful lessons to be learned both in quantifying its effects, and in designing testing methodologies.

One common measurement technique utilized in the study of adhesion is pull-off testing. In pull-off testing, the testing apparatus generally uses a point-contact head to contact the sample (essentially, a hemispherical tip contacting a planar sample, see Figure 17).

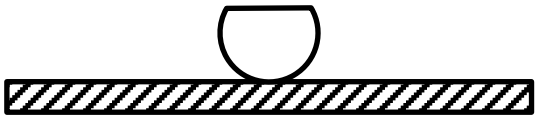

Figure 17. Simple diagram of a point-contact test tip on flat sample.

The adhesive interaction of the tip and the sample can be determined from knowledge of the material properties of each material and of the force required to separate the two. The analysis of this adhesive force is largely derived from contact mechanics, and uses two principle theories. Derjaguin-Müller-Toporov (DMT) theory is a simple extension of basic contact mechanics which incorporates adhesion. It assumes that there is little deformation of the sample and that the adhesive forces are relatively weak [Derjaguin *et al.*, 1975]. In DMT theory, the total force between test tip and sample is the sum of any applied forces and the force of adhesion. The force of adhesion is determined as follows:

$$F_{adh} = 2\pi R_{eff} W_{adh} \tag{47}$$

Here R_{eff} is the effective radius of the contact tip and W_{adh} is the work of adhesion, which can be determined from examination of a force-displacement curve for a particular sample.

As an alternative to DMT theory we consider Johnson-Kendall-Roberts (JKR) theory, which makes greater allowances for deformation in the sample (of interest due to the flexible nature of the polymer samples) [Johnson *et al.,* 1971]. JKR theory incorporates elements of fracture mechanics for characterizing the separation of the tip from the sample, leading to a slightly altered expression for force of adhesion:

$$F_{adh} = \frac{3}{2}\pi R_{eff} W_{adh} \tag{48}$$

The slight discrepancy between JKR and DMT theories is brought on by the different way they approach deformation in the sample. It has been shown, however, that both theories are effective, albeit for different material types. DMT theory serves best when used with stiff materials with lower expected adhesion, while JKR theory works well with strongly adhesive, elastic materials. The implications of each theory as they relate to point-contact pull off theory are discussed in Jacobs *et al.*; for our purposes, ongoing testing has adopted a JKR-based point-contact pull off model, as opposed to the three-point-bending analyzed elsewhere in this paper. [Jacobs *et al.,* 2014].

The change to a pull-off methodology necessitated changes to the testing apparatus and software. We overhauled the structure of the testing apparatus, adapting the test head to accommodate a point-contact tip, as well as reinforcing and insulating the frame of the apparatus to accommodate testing at higher voltages. New data collection capabilities were integrated with the design. Additionally, improvements were made to the control software, allowing for improved test methodologies, more precise data collection, and on-the-fly calculation and plotting of important results, e.g. work and energy of adhesion. These adjustments allow for the force of adhesion to be rapidly computed from the data. With these modifications, testing of

polymers can be completed more rapidly, in more extreme conditions, with higher quality results.

An early outcome of the continued pull-off testing suggests that, contrary to the analysis presented in this paper, there may be a higher-than-expected upper limit to effective stiffness; instead, after a certain voltage, the interactions between polymer layers begin to behave as if there are additional 'virtual layers,' creating further stiffness increases. This alternative model has some basis in literature [Tabata *et al.,* 2001]; investigation of this phenomenon is ongoing.

6.0 SUMMARY AND CONCLUSIONS

In Ladd's work, it was shown that polymer solutions derived from poly(ethylene-*co*-acrylic) acid demonstrated electroadhesive properties, exhibiting increased rigidity when supplied with voltage as a result of the Johnsen-Rahbek effect. Though a positive correlation between voltage and rigidity was established, no concrete relationship was defined. Our first task was finding an empirical model that matched Ladd's empirical results, and extending that model to voltage ranges outside the realm of previously conducted tests. We used an elementary beam bending approach; a simple-to-implement calculation that produced a close fit of the experimental data, without attempting to explain the origin of the results. In short, we divided the sample behavior into three different regimes of beam bending: a low-voltage regime where the layers in a sample are unbonded, an intermediate-voltage regime with some degree of connection between layers, and a high-voltage regime with complete bonding between the layers, producing a single composite beam. The fact such a simple model could accurately predict the results of complex electroadhesive phenomena like the J-R effect was an encouraging result, and formed a useful basis for further adaptation.

For our second pass at developing a model, we incorporated more sophisticated treatment of composite beams. Our investigation of Timoshenko theory as an alternative to elementary bending led to the implementation of sandwich theory, a beam type more representative of our sample geometry. Sandwich beams incorporate rigid faceplates around a less-rigid core layer, an

excellent analogy for our polymer samples between electrodes. We extended the notion of sandwich beams into a “composite of composites” model, where we modelled the behavior of polymer samples as a beam composed of elementary and sandwich-composite sections. This approach raised two key questions – how is the sandwich-composite section oriented, and what are its dimensions?

In part to address these questions, and in part for insight into other types of beam bending, we explored structural engineering literature. This gave rise to the idea of a model which treated the adhesive forces between layers as discrete connectors, like the pins or rods joining concrete or steel beams. Because of the way in which the J-R effect manifests itself, the comparison seemed particularly apt. Research showed that previous investigations had demonstrated the validity of a probabilistic approach to mapping polymer surfaces; by combining the idea of randomly-generated polymer samples with an analysis of concentrated areas of J-R effect, a model for determining the dimensions of a sandwich section was born. The combination of these methods has produced promising results, although further improvement is possible. In particular, a more robust and sophisticated model for polymer surfaces that better-quantifies the areas with intense J-R effects could substantially improve the estimate of the sandwich section dimensions. Additionally, a better understanding of the relationship between our J-R threshold figure and the properties of polymer samples is needed. In particular, our model does not perform uniformly across the studied polymers, and does not adequately capture the performance of samples at higher voltages. Nevertheless, the current iteration is a useful tool for estimating polymer performance at voltages within the ranges currently studied. With further verification and iteration, the principle could be extended to higher voltages, or even alternative polymers.

Finally, while the results presented in this paper are encouraging, some issues remain. While our exploration of adhesion and contact mechanics did not find a place in the composite-of composites model, it did suggest an important change in methodology for producing more reliable results. As a result, additional tests were conducted using pull-off tests as opposed to three-point bending. These additional tests suggest that there may be a higher-than-expected limit to effective stiffness caused by the formation of ‘virtual layers’ at high voltages. Continuing this approach forms an exciting future direction for this work.

BIBLIOGRAPHY

1. Colin Ladd. *Design and Characterization of Electroresponsive Polymers Based on the Johnsen-Rahbek Effect*. Master's Thesis, University of Pittsburgh, 2016.

2. D. Halliday, R. Resnick, & Walker, J. *Fundamentals of Physics,* 8th ed. Published 2007 by John Wiley & Sons, Inc., Hoboken, NJ.

3. R. Atkinson. "A simple theory of the Johnsen-Rabhek effect," *Journal of Physics D: Applied Physics*, Vol. 2, 1969.

4. S. Qin and A. McTeer. "Wafer dependence of Johnsen-Rahbek type electrostatic chuck for semiconductor processes," *Journal of Applied Physics,* Vol. 102, 2007

5. L. Di Lillo, D.A. Carnelli, A. Bergamini, S. Busato, & P. Ermanni. "Quasi-static electric properties of insulating polymers at a high voltage for electro-bonded laminates," Institute of Physics Publishing, Smart Materials and Structures, 2011.

6. R. Cirpriano and J. Longoria. US Patent 5525642, assigned to Dow Chemical Co.

7. A. Ugural and S. Fenster. *Advanced Strength and Elasticity*, 4th ed. Published 2003 by Prentice Hall Professional Technical Reference, Upper Saddle River, NJ.

8. S. Timoshenko. "On the correction factor for shear of the differential equation for transverse vibrations of bars of uniform cross section," *Philosophical Magazine,* 1921.

9. D. Zenkert. *An Introduction to Sandwich Construction.* Published 1995 by Engineering Materials Advisory Services, Warrington, UK.

10. G. Fabbrocino, G. Manfredi, E. Cosenza. "Analysis of continuous composite beams including partial interaction and bond," *Journal of Structural Engineering,* Vol. 126, 2000.

11. EN 1994. *Eurocode 4: Design of composite steel and concrete structures.* 2004.

12. ISO 13918:2008 *Welding. Studs and ceramic ferrules for arc stud welding.* 2013.

13. S. Hicks. *Shear connection in composite beams.* Published 2003 by The Steel Construction Institute, Ascot, UK

14. J. Douglas. “How does surface roughness affect polymer-surface interactions?” *Macromolcules,* Vol. 22, 1989

15. B. Derjaguin, V. Müller, & Y. Toporov. “Effect of contact deformations on the adhesion of particles,” *Colloid Interface Science,* Vol. 53, 1975

16. K. Johnson, K. Kendall, & A. Roberts. “Surface energy and the contact of elastic solids,” *Proceedings of the Royal Society A*, Vol. 324, 1971

17. T. Jacobs, C. Mate, K. Turner, & R. Carpick. “Understanding the Tip-Sample Contact: An overview of contact mechanics from the macro- to the nanoscale,” in *Scanning Probe Microscopy in Industrial Applications: Nanomechanical characterization,* 1st ed. Published 2014 by John Wiley & Sons, Inc., Hoboken, NJ.

18. O. Tabata, S. Konishi, P. Cusin, Y. Ito, F. Kawai, S. Hirai, & S. Kawamura. “Micro fabricated tunable bending stiffness devices,” *Sensors and Actuators A,* Vol. 89, 2001